Twist-Induced Hyperbolic Shear Metasurfaces

Simon Yves,[1,†] Emanuele Galiffi,[1,†] Xiang Ni,[1,2] Enrico M. Renzi,[1] and Andrea Alù[1,3,*]

[1]*Photonics Initiative, Advanced Science Research Center, City University of New York, New York, New York 10031, USA*

[2]*School of Physics, Central South University, Changsha, 410083, China*

[3]*Physics Program, Graduate Center, City University of New York, New York, New York 10026, USA*

(Received 9 October 2023; accepted 22 April 2024; published 24 May 2024)

Following the discovery of moiré-driven superconductivity and density waves in twisted-graphene multilayers, twistronics has spurred a surge of interest in tailored broken symmetries through angular rotations enabling new properties, from electronics to photonics and phononics. Analogously, in monoclinic polar crystals a nontrivial angle between nondegenerate dipolar phonon resonances can naturally emerge due to asymmetries in their crystal lattice, and its variations are associated with intriguing polaritonic phenomena, including axial dispersion, i.e., the rotation of the optical axis with frequency, and microscopic shear effects that result in an asymmetric distribution of material loss. So far, these phenomena have been restricted to specific midinfrared frequencies difficult to access with conventional laser sources and fundamentally limited by the degree of asymmetry and by the strength of light-matter interactions available in natural crystals. Here, we leverage the twistronics concept to demonstrate maximal axial dispersion and loss redistribution of hyperbolic waves in elastic metasurfaces, achieved by tailoring the angle between coupled metasurface pairs featuring tailored anisotropy. We show extreme control over elastic wave dispersion and absorption via the twist angle and leverage the resulting phenomena to demonstrate enhanced propagation distance, in-plane reflection-free negative refraction and diffraction-free defect detection. Our work welds the concepts of twistronics, non-Hermiticity, and extreme anisotropy, demonstrating the powerful opportunities enabled by metasurfaces for tunable, highly directional surface-acoustic-wave propagation of great interest for a wide range of applications spanning from seismic mitigation to on-chip phononics and wireless communication systems, hence paving the way toward their translation into emerging photonic and polaritonic metasurface technologies.

DOI: 10.1103/PhysRevX.14.021031 Subject Areas: Acoustics, Metamaterials

I. INTRODUCTION

Breaking symmetries is paramount to achieving exquisite control over light and sound propagation. A landmark example is found in hyperbolic waves characterized by strongly directional, raylike propagation [1–4] driven by extreme asymmetry in the material response. Such atypical wave dynamics can naturally emerge in polar dielectrics that support hybrid light-matter quasiparticles stemming from the resonant coupling between photons and strong in-plane anisotropic lattice vibrations, namely, hyperbolic phonon polaritons [5–11]. These peculiar surface waves exhibit extreme field confinement, ultralow loss, and highly canalized propagation at midinfrared frequencies, offering exciting opportunities for superior light manipulation, large light-matter coupling, sensing, and imaging at the nanoscale.

In this context, a further degree of asymmetry has been recently unveiled in monoclinic polar crystals, where a new form of surface polaritons emerges from the interaction of light with two nondegenerate dipolar phonon resonances whose orientation forms a nontrivial angle. The resulting hyperbolic shear polaritons are characterized by microscopic shear phenomena that lead to an in-plane rotation of their optical axis with frequency, accompanied by asymmetric damping of the supported hyperbolic waves [12–14]. Compounding the intrinsic directionality of hyperbolic waves with this loss asymmetry leads to a new degree of wave control in nano-optics. While exciting from a fundamental level, natural material platforms supporting hyperbolic shear polaritons suffer from several drawbacks, such as the inherent limitation to midinfrared frequencies for the relevant phonon resonances, difficult to access with commercial lasers, lack of tunability, and restrictions on the degree of asymmetry naturally available in crystal lattices.

*To whom correspondence should be addressed: aalu@gc.cuny.edu

†These authors contributed equally to this work.

These constraints prevent deeper manipulation and control of shear-hyperbolic responses, restraining their range of potential applications.

To overcome these limitations and harness hyperbolic shear waves on demand, here we extend this concept to hyperbolic metasurfaces, structured thin sheets patterned with subwavelength resonator arrays that realize strong in-plane anisotropy, enabling precise control over the symmetries that govern wave propagation, and dramatically enhancing wave-matter interactions [15–19]. As a new paradigm to design hyperbolic shear metasurfaces, given the important role of rotations and asymmetries, it appears natural to embrace the concept of twistronics [20] from condensed-matter systems, based on which the combined rotation and stacking of rotated layered materials can induce exotic responses, such as superconductivity [21] and density waves [22], as well as a variety of new phenomena spanning the fields of electronic [23–26], photonic [27–36], and phononic [37–45] systems. Without loss of generality, here we work with elastodynamic waves, overlaying two thin elastic 3D-printed metasurfaces, each loaded with a different subwavelength array of anisotropic pillar resonators [46]. By leveraging their reconfigurable twist angle, we achieve precise control over shear wave phenomena, demonstrating maximal axial dispersion and mirror-asymmetric lifetime of flexural hyperbolic shear waves. Finally, we leverage the unique properties of hyperbolic shear waves to demonstrate reflectionless negative refraction at an interface, and propose a technological avenue for this concept to realize axial-dispersion-based surface scanning for diffraction-free nondestructive testing.

By combining the concepts of non-Hermicity and twistronics, our results establish an intuitive, general paradigm for the realization and control of twist-governed monoclinic hyperbolic metasurfaces extendable across multiple wave domains. Beyond the experimental demonstration of hyperbolic shear phenomena, our elastodynamic platform paves the way for advanced surface-wave technologies ranging from on-chip phononics to seismic mitigation [46,47], as well as metasurface-based devices for radio-frequency telecommunications and nanophotonic technologies [48,49].

II. MONOCLINIC HYPERBOLIC METASURFACE

Consider an elastic metasurface formed by an array of subwavelength unit cells, each featuring two dipolar resonances R_1 and R_2. Their respective Lorentzian response functions $\tau_1(\omega)$ and $\tau_2(\omega)$ account for their hybridization with the flexural waves of a thin plate (equivalent to the dielectric permittivity of a polaritonic material), for an excitation oriented along their oscillator directions. If the two resonators are orthogonal, the resulting linear response tensor $\hat{\tau}$ is uniaxial, with different diagonal components $\tau_{xx} = \tau_1$ and $\tau_{yy} = \tau_2$, and null off-diagonal terms $\tau_{xy} = \tau_{yx} = 0$ defined in a Cartesian reference frame whose axes x and y are aligned with the resonator symmetry axes [Fig. 1(a), left]. In the absence of absorption, the elements of $\hat{\tau}$ are Hermitian and, if the two resonances are nondegenerate, a band between the two resonance frequencies emerges, within which τ_{xx} and τ_{yy} have opposite signs. In this frequency range, the metasurface supports hyperbolic elastic waves, in analogy to the hyperbolic polaritons demonstrated in various uniaxial polar crystals in their reststrahlen bands [9–11].

We assume a general Kirchoff-Love model for flexural (i.e., antisymmetric) $A0$ modes supported by a thin plate, which we assume to be decoupled from the (symmetric) $S0$ mode, and consider its coupling to a subwavelength array of pillar resonators. In the Supplemental Material [50] Secs. I and II, we derive and solve a homogeneous model that accounts for the interaction of the resonators with the flexural displacement field of the plate. The eigenmodes of the system consist of solutions of the dispersion relation

$$D\Delta^2 w + \vec{\nabla} \cdot (\hat{\tau} \vec{\nabla} w) - \rho h \omega^2 w = 0, \tag{1}$$

where h is the plate thickness, ρ the plate (volume) mass density, $D = Eh^3/12(1-\nu^2)$ the plate stiffness with the Young's modulus E and Poisson ratio υ, and Δ corresponds to the Laplacian operator. For simplicity, in Fig. 1 we restrict ourselves to the local (small-wave-vector) limit $D \to 0$, which is homomorphic to a 2D model for the electromagnetic scalar potential, as detailed in Appendix C. For $\tau_1\tau_2 < 0$, the modes form hyperbolic isofrequency contours (IFCs) in momentum space, with principal axis (the symmetry axis crossing the tip of the hyperbola) aligned with the resonators [the dotted line in the right panel of Fig. 1(a) accounts for the three overlapping axes], but frequency-dependent asymptotes [blue to green contours in Fig. 1(a)], consistent with the open-angle dispersion of hyperbolic phonon polaritons in uniaxial crystals [9–11].

Consider now nonorthogonal resonators, such that R_1 is aligned with the x axis, while R_2 forms an angle θ with it [Fig. 1(b)]. The linear response tensor becomes (see Supplemental Material Sec. I [50])

$$\hat{\tau} = \begin{pmatrix} \tau_1 + \tau_2\cos^2(\theta) & -\tau_2 \sin(\theta)\cos(\theta) \\ -\tau_2 \sin(\theta)\cos(\theta) & \tau_2\sin^2(\theta) \end{pmatrix}. \tag{2}$$

The nonzero off-diagonal terms are responsible for the interaction between the two resonators due to their nonorthogonality. This coupling leads to axial dispersion, namely, a frequency-dependent rotation of the principal axis [dotted lines in Fig. 1(b)] and of the hyperbolic IFCs, by an angle (see Appendix B for details)

$$\beta = \frac{1}{2}\tan^{-1}\left[\frac{\Re[\tau_2]\sin(2\theta)}{\Re[\tau_1] + \Re[\tau_2]\cos(2\theta)}\right], \tag{3}$$

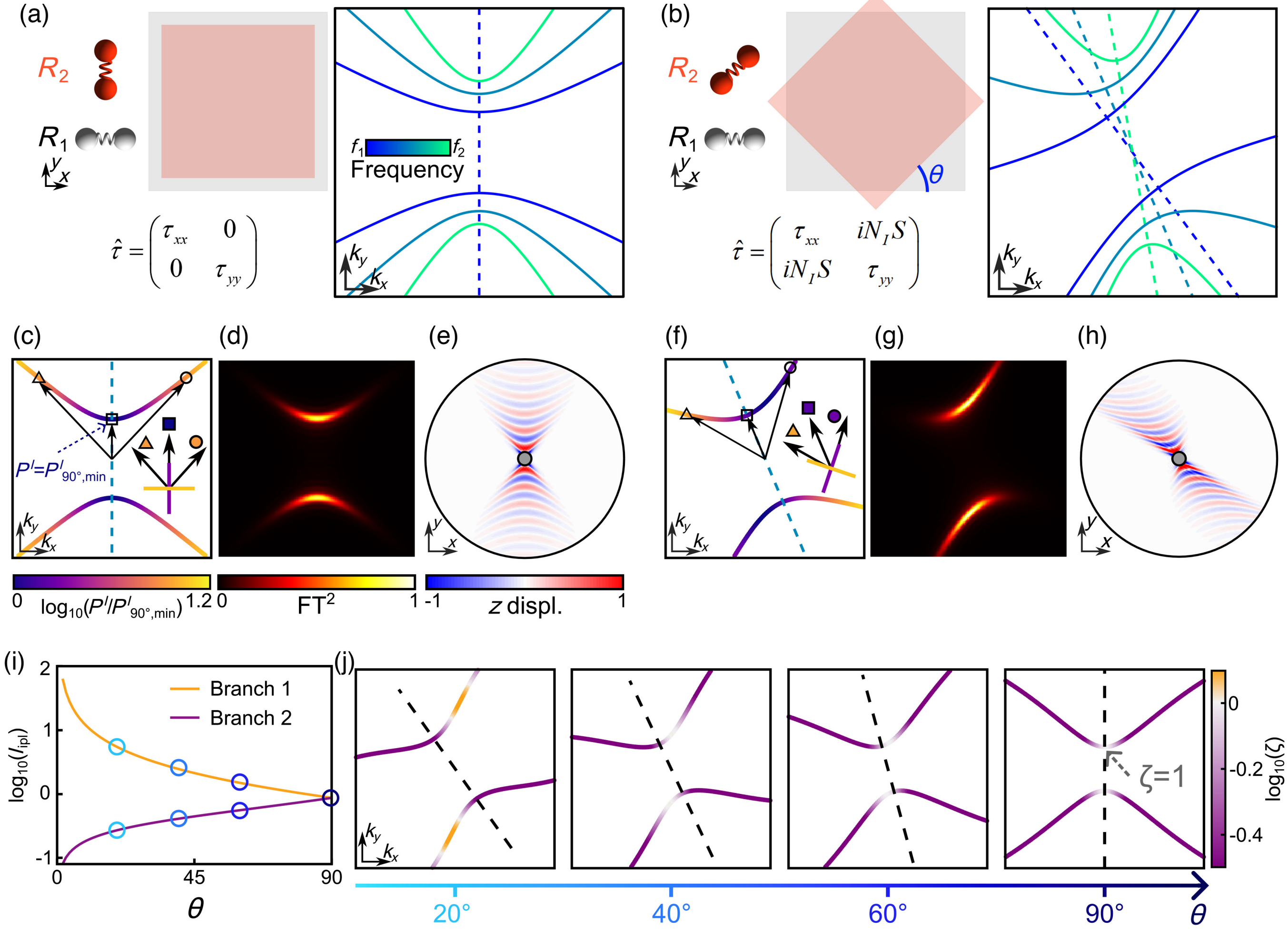

FIG. 1. Twist-induced axial dispersion and loss asymmetry. (a) A metasurface formed by orthogonal dipolar resonators R_1 and R_2 is described by a diagonal tensor $\hat{\tau}$, leading to a frequency-independent principal axis (dotted line). (b) By contrast, a twist angle $0° < \theta < 90°$ (45° in this example) between the two dipolar resonators introduces off-diagonal terms in the tensor $\hat{\tau}$, resulting in axial dispersion, i.e., frequency dependence of the principal axis orientation (dotted lines). (c)–(e) Considering the non-Hermitian features of $\hat{\tau}$, the orthogonal scenario shown in (a) leads to (c) conventional axisymmetric loss profiles (logarithmic color scale shows the power loss rate P^I normalized to the lowest-loss state for $\theta = 90°$), also evidenced in the (d) reciprocal and (e) real-space hyperbolic polariton propagation under near-field excitation (gray disk). Note how in conventional hyperbolic media the large momentum states suffer from large losses. (f)–(h) The change in relative angle between the principal axis and the underlying resonators depicted in (b) yields (f) asymmetric loss profiles leading to enhanced directionality in polariton propagation along one of the hyperbolic arms shown in (g) reciprocal and (h) real space. Insets in (c) and (f) show, respectively, the symmetric and asymmetric loss stemming from the alignment or misalignment between the eigenvectors of $\mathfrak{I}[\hat{\tau}]$ (orange and purple segments denote high- and low-loss eigenvectors of $\mathfrak{I}[\hat{\tau}]$) and the field eigenvectors (black arrows) corresponding to three eigenvalues (shaped markers) located symmetrically with respect to the principal axis. (i),(j) The lifetime enhancement induced by the twist angle is evident from (i) the line integral of the lifetime along the two arms of the dispersion hyperbola, and (j) the ratio $\zeta = P^I_{90°,\mathrm{min}}/P^I$ [enlarged compared to (c),(f); see also Fig. S11 in Supplemental Material [50]) between the lifetime of each state and the maximum lifetime for the conventional hyperbolic polariton shown in panels (a),(c)–(e) plotted for different angles (blue color scale). Note how the redistribution of loss endows high-momentum states on one branch with remarkably long lifetimes.

obtained by diagonalizing $\hat{\tau}$, consistent with the recently observed axial dispersion of hyperbolic shear polaritons in monoclinic crystals [12–14].

Once material losses are included in the oscillator responses $\tau_1(\omega)$ and $\tau_2(\omega)$, $\hat{\tau}$ becomes non-Hermitian, and the losses of each mode can be evaluated via the power loss rate $P^I = \nabla w^{\dagger} \mathfrak{I}[\hat{\tau}^{\dagger}] \nabla w$ (see Appendix C and Supplemental Material Sec. III for details [50]). This power loss rate is shown in Fig. 1(c) normalized with respect to the least lossy state for the orthogonal ($\theta = 90°$) case, i.e., the state at the vertex of the dispersion hyperbola. For orthogonal oscillators ($\theta = 90°$), the loss distribution inherits the symmetry axis of the contour [dotted line in Fig. 1(c)], indicating that mirror-symmetric modes are equally long-lived. Hence, a point source excites the four hyperbolic branches with equal efficiency, yielding mirror-symmetric features in reciprocal and real space, as shown in Figs. 1(d) and 1(e), respectively.

By stark contrast, in a monoclinic system ($\theta \neq 90°$) the principal axis associated with the Hermitian contribution of the material response cannot be generally expected to be a symmetry axis for the dissipative processes affecting the modes. Consequently, in the frame aligned with the symmetry axis of the contour, only the real part of the tensor $\hat{\tau}' = \hat{R}(\beta)\hat{\tau}\hat{R}(\beta)^T$ is diagonal, resulting in purely imaginary off-diagonal elements τ'_{xy} in the rotated frame. This quantity measures the misalignment between the symmetry axes of the Hermitian and non-Hermitian components of the tensor $\mathfrak{R}[\hat{\tau}]$ and $\mathfrak{I}[\hat{\tau}]$, which leads to a mirror-asymmetric distribution of the loss along the contours exemplified in Fig. 1(f) (see Appendix D and Supplemental Material Sec. IV [50]), consistent with recent observations for hyperbolic shear polaritons [12–14]. Normalizing τ'_{xy} by the total loss in the system yields the shear factor $S(\omega, \theta)$. Despite being agnostic to the IFCs of the system, the shear factor is proportional to the difference between the power loss rate calculated at any two mirror-symmetric k points of a given contour, making it the relevant criterion for quantifying the strength of loss asymmetry (see Supplemental Material Sec. IV for details [50]). Geometrically, this effect is associated with the misalignment between the eigenfields mirrored with respect to the principal axis [arrows in Figs. 1(c) and 1(f) and insets] and the eigenvectors of the non-Hermitian component of $\hat{\tau}$ [orange and purple segments in Figs. 1(c) and 1(f) insets denote high-loss and low-loss eigenstates of $\mathfrak{I}[\hat{\tau}]$ respectively]. Importantly, the shear factor $S(\omega, \theta)$ is independent of the absolute loss in the system, as can be seen by multiplying $\mathfrak{I}[\tau_1]$ and $\mathfrak{I}[\tau_2]$ in Eq. (D4) by a common factor (Appendix D).

Because of this broken symmetry, a point source will selectively excite the two low-loss hyperbolic branches, as evident from Fig. 1(g), producing a remarkably skewed, and more directional, hyperbolic wave [Fig. 1(h)]. Notably, this angular redistribution of loss enables a dramatic extension in the lifetime of modes carrying large momenta, as opposed to the conventional hyperbolic case of Fig. 1(d), despite the overall dissipation in the resonators being the same. In turn, this implies that the corresponding shear-hyperbolic waves can propagate much farther, and more directionally, than in the case of mirror-symmetric hyperbolic waves in Fig. 1(e), establishing twistronics as a powerful paradigm to tailor ultralong-lived shear-hyperbolic waves. To quantify this enhancement in propagation length, Fig. 1(i) shows the logarithm of the lifetime integrated over the two arms of the dispersion hyperbola as a function of the twist angle, demonstrating an overall enhancement across the entire arm of the hyperbola of multiple orders of magnitude. Remarkably, the integrated lifetime grows monotonically for one arm of the hyperbola and decreases for the other. Furthermore, Fig. 1(j) shows the twist angle dependence of the lifetime enhancement factor $\zeta = P^I_{90°,\min}/P^I$, i.e., the ratio between the lifetime of the hyperbolic waves in the shear metasurface at each k point, and the maximum lifetime of the conventional hyperbolic waves at the vertex of the dispersion hyperbola in Figs. 1(a) and 1(c)–1(e). It is therefore evident how our shear metasurface can leverage the twistronics paradigm to dramatically enhance the propagation of hyperbolic waves, both at the modal level and for the integrated response.

III. TWISTED-BILAYER ELASTIC METASURFACES

In order to validate our theory and demonstrate these phenomena, we fabricate a mechanical metasurface consisting of two 3D-printed thin plates, each loaded with an array of rectangular pillars [Fig. 2(a); see fabrication details in Appendix A and Fig. S1 of Supplemental Material [50]], whose respective heights h_1 and h_2 are offset to detune their directional bending resonances. In turn, they support a hyperbolic frequency band with effective resonant material response $\mathfrak{R}[\tau_1(\omega)] < 0$ and $\mathfrak{R}[\tau_2(\omega)] > 0$ [Fig. 2(b); see also Supplemental Material Sec. I [50]]. The two plates are coupled using double-sided tape [inset in Fig. 2(a)], enabling full control over the twist angle θ between the oscillation axes of the detuned resonators in each layer.

In order to model the elastic response, we use the full nonlocal thin-plate Kirchoff-Love model outlined in Eq. (1) for the flexural waves. As a result, the analytical IFCs for $\theta = 60°$ [Fig. 2(c)] are not open like usual hyperbolic waves, but form closed hippopedal contours due to the fourth-order spatial derivatives that dominate the dispersion for large momenta. Yet, they feature a local hyperbolic response for realistically achievable wave numbers, and clearly show strong axial dispersion for the three frequencies denoted in Fig. 2(b) by blue-to-green vertical lines within the reststrahlen band. While the IFCs in the lossless scenario follow the symmetry dictated by the principal axes [dashed lines in Fig. 2(c)], axial dispersion alone is not sufficient to capture the simulated [Fig. 2(d); see simulation details in Appendix B] phenomenology arising from point-source excitation, which is in remarkable agreement with the experimental measurements of the twisted metasurface sample [Fig. 2(e)]. This insufficiency is due to the broken mirror symmetry in the loss distribution: As visible from the Fourier (left columns) and real (right columns) space plots, the excitation profile is very skewed, evidencing the shear features of the hyperbolic waves. This loss asymmetry closely matches our analytical prediction in Fig. 2(c). Notably, this asymmetry, stemming from shear phenomena, does not hinge on the hyperbolic nature of the bands, but it arises regardless of the contour topology. Based on the previous discussion, it is due to the interplay between monoclinicity and non-Hermiticity of the effective response tensor $\hat{\tau}$ of the metasurface. Its implementation

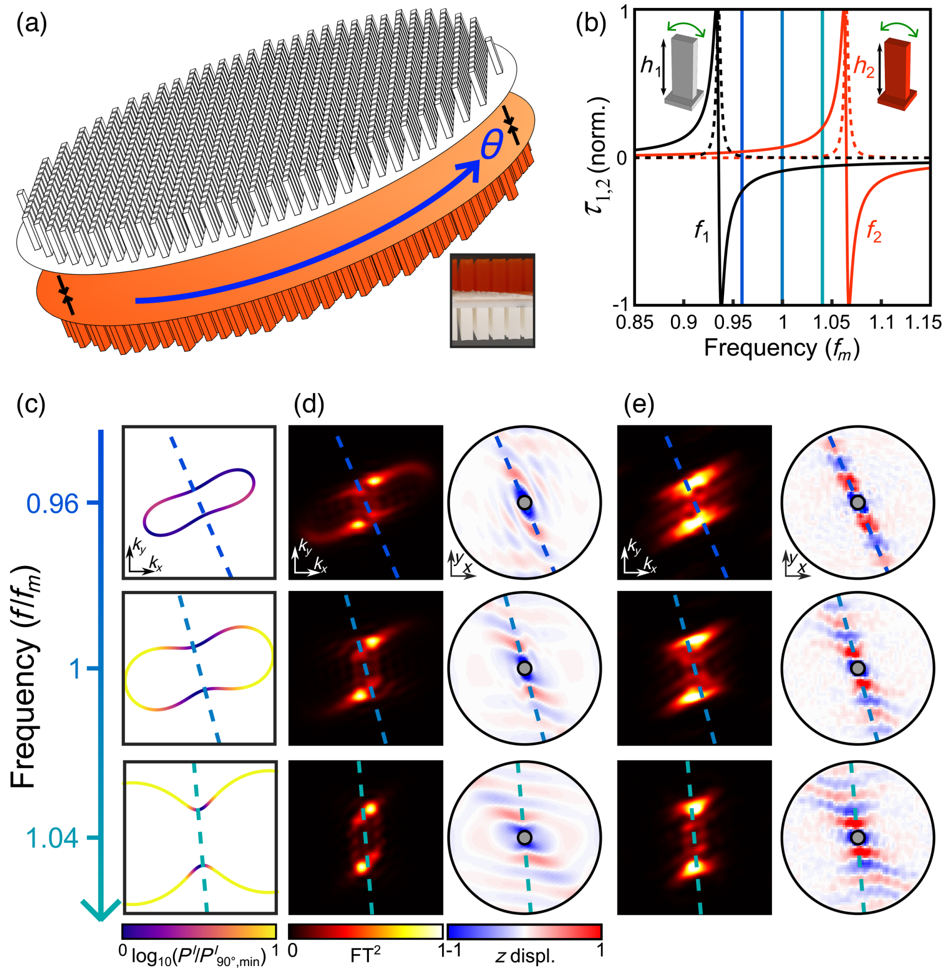

FIG. 2. Twisted elastic metasurface. (a) Illustration of back-to-back-stacked elastic metasurfaces twisted by an angle θ. The inset shows a cross section of the experimental sample. (b) Frequency dependence of the effective linear response parameters τ_1 and τ_2 for two detuned pillar-bending resonators of height $h_1 = 7.5$ mm and $h_2 = 7.0$ mm (inset) normalized by the center frequency $f_m = (f_1 + f_2)/2$. (c) Analytic IFCs of our homogenized elastic metasurfaces for $\theta = 60°$ and different frequencies corresponding to the blue-to-green lines in (b). The contour color scale indicates the corresponding normalized power loss rate (increasing from purple to yellow) $P^I/P^I_{90°,\mathrm{min}}$. Dashed lines denote the principal axis at the three frequencies chosen in (c). (d) Finite-element simulations of the flexural displacement of the pillar system under point-source excitation (gray disk) demonstrate axial dispersion and loss asymmetry in Fourier (left) and real (right) space. (e) Corresponding displacement measurements carried out with a laser vibrometer, showing excellent agreement. The spatial scale of all real-space plots corresponds to the diameter of the sample (51 unit cells of 3.5 mm each), while Fourier maps extend over $0.48\pi/A \approx 0.431$ rad/mm.

using a design as intuitive as twisted metasurfaces opens a plethora of opportunities for advanced integrable and reconfigurable devices in phononics and photonics.

IV. MAXIMAL AXIAL DISPERSION AND SHEAR FACTOR

We now quantify and maximize axial dispersion and loss asymmetry in our twisted hyperbolic shear metasurfaces. Figure 3(a) shows the theoretically predicted rotation angle β as a function of the frequency for different twist angles θ. Notice how the axial rotation becomes increasingly abrupt as the twist angle is reduced, enabling control over both range and rate of axial dispersion with the frequency. Interestingly, the behavior of β with respect to θ can be found in two distinct phases, depending on the dominant oscillator. At low frequencies ($|\mathfrak{R}[\tau_1]| > |\mathfrak{R}[\tau_2]|$), the principal axis fully rotates together with the twist angle between the dipolar resonators, ranging from 0° to 90°. Conversely, at high frequencies ($|\mathfrak{R}[\tau_2]| > |\mathfrak{R}[\tau_1]|$), the principal axes tilt only up to a finite angle, and then revert to their original orientation along the x axis (see Fig. S2 of Supplemental Material [50] for more details). The existence of this phase transition highlights the importance of the transition frequency $f \approx f_m$ [black dotted line in Figs. 3(a) and 3(b)], at which $|\Re[\tau_1]| \approx |\Re[\tau_2]|$. In fact, the similarity between the two detuned oscillator strengths in this transitory regime implies a stronger interaction between

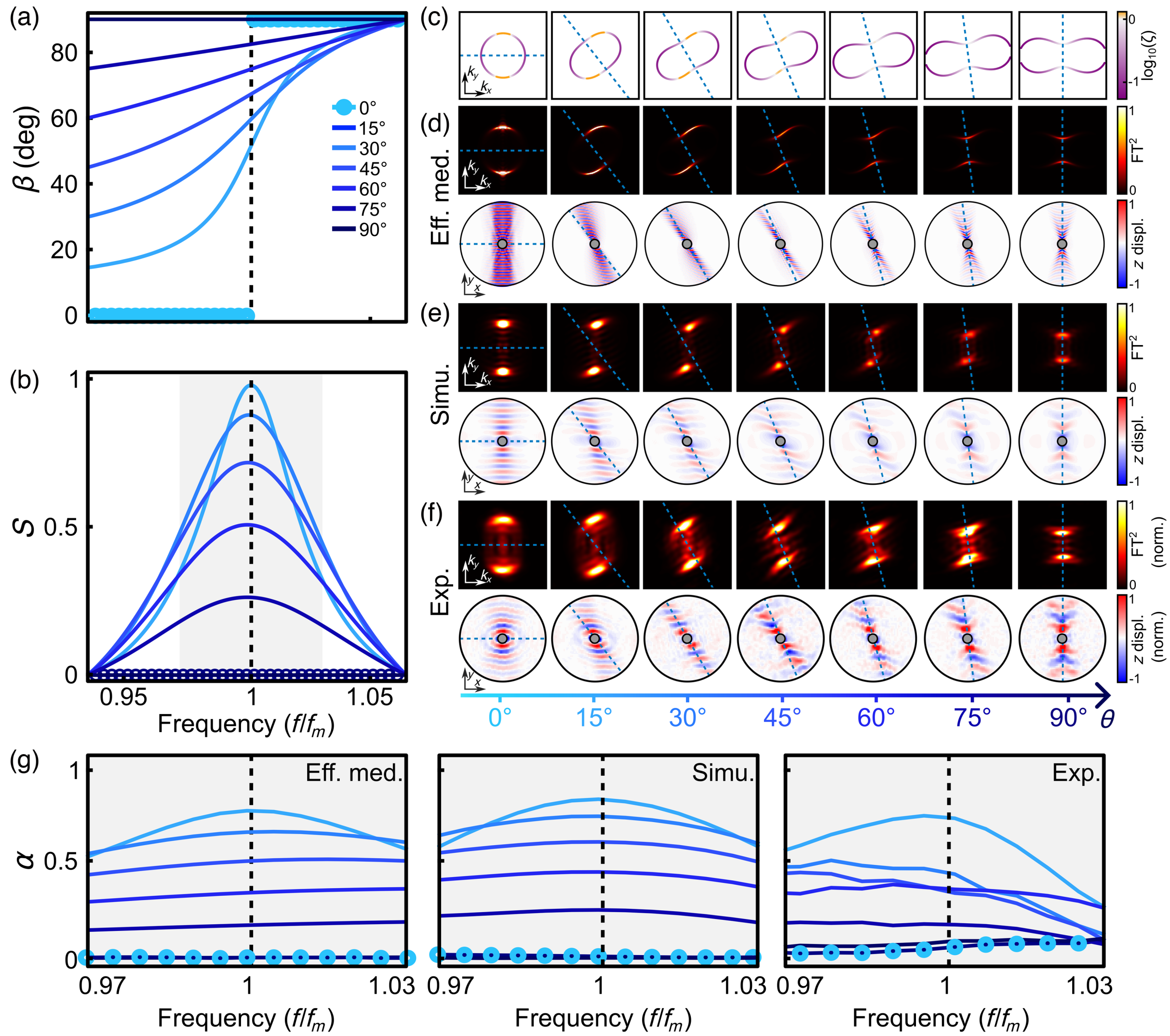

FIG. 3. Maximal axial dispersion and loss asymmetry tuning with twist angle and frequency. (a) The frequency dependence of the principal axis angle β for different twist angles θ (blue shades) reveals an axial winding phase (lower frequencies), whereby the axis fully rotates by 90° as θ varies from 0° to 90°, and an axially stable phase (higher frequencies), whereby the principal axis rotates but then folds back. (b) This behavior strongly impacts the bandwidth of the shear factor S, which peaks at the transition frequency f_m [dotted black line in (a),(b)], where the interaction between the two resonant modes is strongest. (c) Twist dependence of theoretical IFCs at the frequency where the shear factor is maximum. (d) Effective-medium theoretical wave propagation results both in reciprocal (top) and real (bottom) space for a large domain, corresponding to the IFCs displayed in (c). (e),(f) Simulation (e) and experimental (f) counterparts of the results presented in (d) for a smaller domain. Dashed lines in (c)–(e) denote principal axes. The spatial scale of the real-space plots for experimental data and pillar simulations corresponds to the diameter of the sample (51 unit cells of 3.5 mm each), whereas homogenized simulations extend over 3.36 times the sample size to show more clearly the enhancement in propagation length. All Fourier maps extend over $0.48\pi/A \approx 0.431$ rad/mm. (g) The asymmetry factor obtained by dividing the difference between the intensities of the Fourier transform of the fields across opposite quadrants by their sum, analogous to Ref. [14], shows an experimental asymmetry peak $\alpha_{\mathrm{max,exp}} = 0.73$ for $\theta = 15°$ at the critical frequency, as predicted by our theory, constituting an asymmetry enhancement of approximately 100% compared to the best experimental values in Ref. [14].

the two resonances, whose balanced interplay maximizes axial dispersion (see Supplemental Material Sec. V [50] for details). This axial dispersion has direct consequences on the degree of loss asymmetry, as shown by the behavior of the shear factor S depicted in Fig. 3(b), which is indeed maximized when $f \approx f_m$ for all nonorthogonal twisted configurations, while its value increases at the expense of its bandwidth following the progressive alignment of the two resonators. This behavior is consistent with the corresponding symmetry breaking in the spatial distribution of losses in the medium, making the twist between metasurfaces a straightforward parameter for the precise control of both strength and bandwidth of the loss asymmetry of shear-hyperbolic waves.

To showcase such versatility, we focus on the regime of maximum shear factor at frequency $f = f_m$, for which the corresponding theoretical IFCs are displayed as a function of the twist angle θ in Fig. 3(c). In particular, for θ changing from 90° to 45°, the contour rotation as a function of the twist angle is accompanied by a sharp increase of the loss asymmetry. As a direct consequence, strongly directional shear-hyperbolic waves exhibit a dramatic increase in propagation length along the suppressed-loss branch as the twist angle decreases, as evidenced by the theoretical field maps of Fig. 3(d) [top (bottom) in reciprocal (real space)]. As the amount of dissipation in the resonators is constant throughout the twisting process, this effect emerges from the redistribution of loss induced by the finite twist angle: While parts of the contours are overdamped, their mirrored counterparts are strongly enhanced compared to the orthogonal hyperbolic case. In reciprocal space, this effect yields a clear sharpening of the corresponding contours [Fig. 3(d), top]. Furthermore, in Fig. S9 of the Supplemental Material [50] we show experimental measurements and simulations of the pillar systems for $\theta = 90°$ and $\theta = 0°$ at the critical frequency to characterize the losses in our metasurface, and we demonstrate a measured 15% enhancement of the relative propagation length of the macroscopic polaritons in the $\theta = 0°$ case compared to the $\theta = 90°$ case. Although significantly smaller than the fivefold enhancement predicted by the numerical simulations for the full pillar system, it is meaningful that the $\theta = 0°$ case hosts states with much shorter wavelengths, which are much more susceptible to losses, roughness, and fabrication defects.

Twisting the metasurfaces even further ($0° \leq \theta < 45°$) induces a topological transition of the contours from quasihyperbolic ($\theta = 45°$) to flat ($\theta = 30°$) and finally elliptic ($\theta \leq 15°$), as the resonators progressively align. In this regime, we find the maximum asymmetry in the loss distribution, corresponding to a shear factor $S \to 1$ for a passive medium, as predicted by our theory in Fig. 3(b), and clearly verified by our simulations and experimental measurements in Figs. 3(c)–3(e) ($\theta = 15°$), where the measured signal strikingly lies entirely on one side of the principal axis. These results are further corroborated by the remarkable agreement of simulations and experiments [Figs. 3(e) and 3(f), respectively].

It is meaningful to compare the degree of asymmetry achieved with our tunable metasurface to those observed in natural materials [13,14]. The asymmetry in the field distribution is fully quantified in Fig. 3(g), where we plot the figure of merit α obtained by subtracting the surface integral of the Fourier map intensity over opposite quadrants defined by the symmetry axis and its normal, and dividing the result by their sum (see Supplemental Material Sec. IV [50] for details). This figure of merit was used in Ref. [14] to quantify the strongest loss asymmetry observed to date, exhibited by shear polaritons in beta gallium oxide. Computing this figure of merit for our measurements and simulations allows us to demonstrate how our design paradigm for shear metasurfaces yields a value of $\alpha \approx 0.75$ corresponding to a loss asymmetry enhancement of approximately 100% compared to the experimental value therein, under perfectly symmetric excitation. Thus, by combining the maximization of the loss asymmetry and the axial dispersion, twisted hyperbolic shear metasurfaces unlock complete control over the wave directionality, while enabling extremely long-range directional steering of hyperbolic waves.

V. REFLECTION-FREE NEGATIVE REFRACTION AT A HYPERBOLIC SHEAR INTERFACE

The interplay between mirror-asymmetric loss distribution and hyperbolicity at a boundary offers unique opportunities to tailor hyperbolic wave propagation and scattering. As an example, it is well known that hyperbolic media exhibit negative refraction at an interface with elliptic media [1,54,55] [Fig. 4(a)]. Indeed, parallel momentum conservation at the interface [represented by a dotted line in Fig. 4(a)] combined with the curvature inversion between isotropic and hyperbolic contours, results in a reflected wave and a negatively refracted one [green arrows denote energy flow in Fig. 4(a)]. This configuration can be implemented using our bilayer metasurface with aligned top and bottom lattices ($\theta = 0°$) in an orthogonal hyperbolic phase interfaced with an unloaded plate forming the isotropic medium [Fig. 4(b)]. Figure 4(c) shows simulations (left) and experimental results (right) that demonstrate the resulting conventional negative-refraction-mediated focusing of the field emitted by a point source placed in the hyperbolic medium and its backreflections.

Negative refraction at an interface has also been recently demonstrated using Weyl metamaterials [56]. Remarkably, due to their topological features it was shown that their dispersion features truncated hyperbolic contours with only half of the branches available, resulting in reflectionless negative refraction at the interface with an elliptic medium. Remarkably, our twist-induced hyperbolic shear waves yield a similar effect: Here the strongly asymmetric damping of the IFCs extends the propagation of one hyperbolic branch [green arrows in Fig. 4(d)], while dramatically hampering the other one [red arrows in Fig. 4(d)], thus supporting negative refraction at the interface without reflections. We verify this prediction with the setup in Fig. 4(e), where loss asymmetry is induced with a $\theta = 30°$ twist between the two layers (inset). In this scenario, the field emitted by the point source propagates only along one of the hyperbolic branches before negatively refracting at the interface, while the reflected wave is strongly attenuated [Fig. 4(f); see also Fig. S5 in Supplemental Material [50] for a comparison between the cases with and without shear]. Although this effect does not guarantee unitary transmission as with Fermi arcs [56], the enhancement in propagation length of the desired mode combined with the

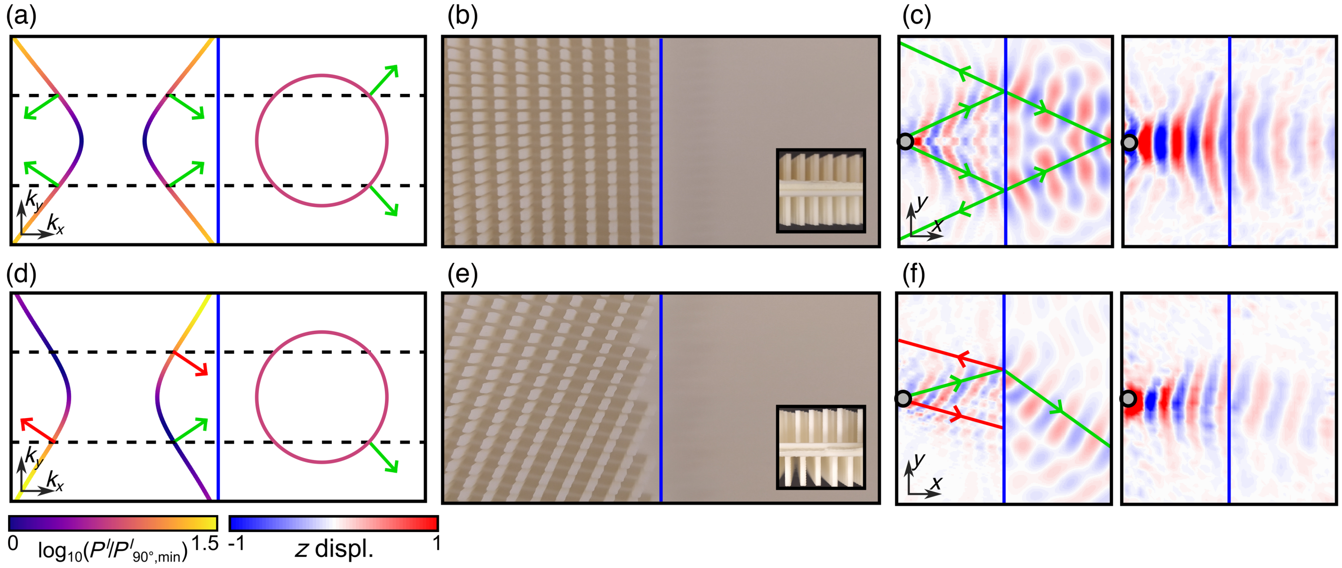

FIG. 4. Shear-induced reflectionless negative refraction. (a) Momentum matching at the interface between a hyperbolic (left) and an isotropic medium (right). Parallel momentum conservation at the interface results in reflected and negatively refracted waves (green arrows). (b) Metasurface interface sample corresponding to (a): pillars are aligned on both plate sides (inset) on the left of the interface, while the plate is nude on the right. (c) Pillar metasurface simulation (left) and experimental measurements (right) showing the refocusing of waves emitted by a point source (gray disk) across the interface in (b), accompanied by backreflections (energy flux is shown as green arrows). (d) In the presence of shear, only one set of waves on the right hyperbolic branch reaches the interface (green arrow), and the reflected waves are heavily damped (red arrow on left branch). (e) Metasurface interface sample corresponding to (d) with a twist angle $\theta = 30°$ (inset) for hyperbolic shear waves. (f) Simulation (left) and measurement (right) of the sample in (e) showing reflectionless negative refraction. The unit cell size in panels (b) and (e) is 3.5 mm as in the rest of the paper, while the size shown in the field plots is 50 unit cells.

suppression of unwanted interference between incoming and reflected signals can greatly aid practical applications, e.g., for imaging. This additional demonstration further highlights the exciting potential of twist-induced shear phenomena for extreme wave manipulation.

VI. DIFFRACTION-FREE DEFECT DETECTION BASED ON HYPERBOLIC AXIAL DISPERSION

We conclude by demonstrating the use of shear-hyperbolic elastic metasurfaces for diffraction-free nondestructive testing. In elasticity, a key technological playground is the wave-based detection of mechanical defects. Here we show that the unique combination of extreme directionality and maximal axial dispersion exhibited by our hyperbolic shear metasurfaces provides a new strategy for defect detection. In a conventional nondestructive testing setup, a material is scanned using complex tomographic techniques and multiple sources and detectors to localize the presence of defects. Hyperbolic waves, thanks to their extreme directionality and subdiffractive propagation features, offer interesting opportunities in this context. However, conventional hyperbolic materials support directional waves limited to a narrow angular range, limiting their potential for defect detection. Shear-hyperbolic metasurfaces, on the contrary, offer axial dispersion, based on which highly directive hyperbolic waves rotate their symmetry axes by varying the excitation frequency. As a result, a broadband excitation can launch a broad range of directional waves, whose angular spectrum is encoded into the excitation frequency, and which can be used to locate defects over a surface.

We provide a proof-of-principle demonstration of this concept in Fig. 5. Figure 5(a) shows a defect-loaded surface. The source is located at the center of the sample, while a defect is realized by removing a few pillars (see Fig. S6 in Supplemental Material [50] for details). Figure 5(b) shows (top) simulated and (bottom) experimentally measured field maps of the vertical displacement of the plate at different frequencies (left to right). The defect location is marked with a semitransparent white circle. Note the large steering of the directive hyperbolic beams with frequency, which spans an angle of approximately 45° within a frequency scan of only 8% of the center frequency f_m of the hyperbolic band (see Fig. S7 in Supplemental Material [50] for details). Figure 5(c) shows the (top) theoretical and (bottom) experimental radiation patterns measured along the black circle in Fig. 5(a) for different frequencies [blue to green; see Fig. 5(b)], clearly showing the shadow created by the defect. Note, however, how the propagation of the waves away from the defect is diffractionless across the entire frequency band considered, since all of the scattered

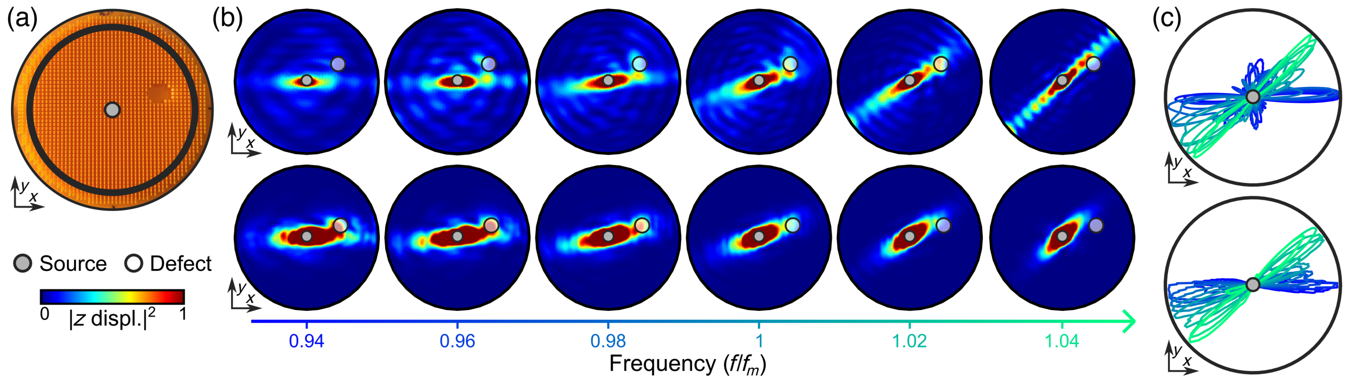

FIG. 5. Diffraction-free nondestructive defect detection based on axial dispersion. (a),(b) The maximal axial dispersion of hyperbolic shear metasurfaces ($\theta = 30°$) is leveraged to detect the location of a surface defect using a fixed point source via frequency steering. In our experimental sample (a), we introduce a localized defect by removing a few pillars on both sides. Panel (b) shows (top) simulated and (bottom) experimental field intensity maps for different excitation frequencies, demonstrating broad steering of subdiffractive flexural waves by approximately 45°. We can precisely locate the defect (semitransparent white circle), thanks to the raylike propagation of hyperbolic waves and their axial dispersion. (c) Simulated (top) and measured (bottom) radiation patterns (green to blue) obtained by averaging the field intensities in the black-shaded area in (a) for each angle, clearly showing the shadow created by the defect. Theoretical and experimental field plot sizes correspond to the diameter of the entire sample approximately 178.5 mm.

waves propagate only along the directions imposed by the hyperbolic bands for each specific frequency. This raylike propagation preserves the resolution with which the information carried by the shadow is measured at the detector. A sketch of the proposed defect detection protocol is given in Fig. S8 of Supplemental Material [50]. Note the contrast between the unobstructed patterns in the lower left quadrant, which evenly scan the entire quadrant, and those in the upper right one, where the defect is located. Remarkably, hyperbolic shear waves support directionality encoded in the operating frequency; hence, they can be dynamically steered without mechanical motion or bias, a concept that can be readily translated to airborne acoustics, photonics, and other wave sciences for sonar and radar applications.

VII. CONCLUSIONS

In this work, we have demonstrated hyperbolic shear waves with maximal axial dispersion and shear phenomena enabled by twisted-bilayer metasurfaces. Our model has highlighted how the interplay of twistronics, non-Hermiticity, and extreme anisotropy endows these metastructures with new forms of wave propagation and loss redistribution, enhancing propagation along certain directions, while hampering it along others. Notably, we have demonstrated that maximizing the loss asymmetry by simply tuning the twist angle allows us to drastically extend hyperbolic wave propagation far beyond the distance expected for a given level of material loss. Furthermore, we have demonstrated applications of shear metasurfaces to achieve extraordinary wave phenomena such as reflectionless negative refraction, as well as a new technological paradigm for nondestructive testing based on axial dispersion. While we have demonstrated these concepts in a low-cost, elastodynamic platform to aid reproducibility of our results, our paradigm for shear-hyperbolic waves is rooted in the breaking of symmetry through twisting and is therefore extendable to a wide range of metamaterial structures and wave domains. For instance, switching to lower-loss aluminum samples would dramatically enhance the lifetime of the waves studied here [57], opening a pathway for reconfigurable on-chip elastic surface-wave devices analogous to their recently proposed electronic counterpart [58]. Moreover, our metasurface design model can be readily used to engineer optical, microwave, or airborne acoustic shear metasurfaces. We believe that our results open a pathway toward twistronics to harness the combined effect of anisotropy and non-Hermitian physics to achieve highly directional, long-range wave control in artificial media.

ACKNOWLEDGMENTS

S. Y., X. N., E. M. R., and A. A. acknowledge funding from the Office of Naval Research, Simons Foundation and the Air Force Office of Scientific Research. E. G. acknowledges funding from the Simons Foundation through a Junior Fellowship of the Simons Society of Fellows (Grant No. 855344, EG).

APPENDIX A: SAMPLE FABRICATION AND EXPERIMENTAL SETUP

Mechanical samples depicted in Figs. S1(a) and S1(b) in Supplemental Material [50] are 3D printed with polylactic acid (PLA; $E \approx 2.5$ GPa, $\nu \approx 0.3$, $\rho \approx 1300$ kg m^{-3}) using the fused deposition modeling technique (3D printer model is Raise3D Pro2 Plus). Although PLA exhibits non-negligible viscoelasticity, which is associated with loss, it is a conventional prototyping material, thanks to its affordable cost and accessibility with standard 3D printers (our samples are printed in-house). This choice benefits the reproducibility of our results without impacting the evidence of our proof-of-principle demonstration of shear-hyperbolic metasurfaces. Lower-loss samples can, in principle, be realized with more expensive metal structures, enabling the realization of technologically more competitive devices. In addition, interlayer coupling constitutes a significant loss channel. Good interlayer coupling is needed to be able to use the homogenized model accurately. In our case, this condition is well satisfied; however, it is easily possible to build even lower-loss samples by gluing the two plates directly with epoxy, which however hinders the reconfigurability aspect, which allows us to repeat the study by simply twisting the same two samples. Adding an extra layer between the two plates would enable better control of the interlayer coupling and loss properties by choosing its structure, composition, and thickness, as demonstrated, e.g., in the realization of a magic-angle flat-band phononic analog of twisted-bilayer graphene using $LiNbO_3$ plates and a rubber spacer (see Ref. [44]).

The cross section of the pillar resonators is 1.225×2.625 mm^2, the lattice step is $A = 3.5$ mm, and the thickness of each PLA plate is 1.3 mm. The diameter of the plates corresponds to 51 unit cells, so that its size is 178.5 mm. These parameters define the frequency range of the pillar resonances and the dispersion of the modes of the nude plate, which hybridize to form the effective polaritonic bands discussed in the main text. Further details on the physics of pillar resonators may be found in Ref. [46]. The out-of-plane displacement field maps of the bilayer metasurface are measured every 10 Hz between 2 and 12 kHz thanks to a 3D laser vibrometer (Polytec PSV-500-3D in spectrum mode), as presented in Fig. S1(c) of Supplemental Material [50]. The medium is excited close to its center thanks to a mechanical shaker (B&K type 4810) and a pointer [Fig. S1(d) in Supplemental Material [50], with a broadband signal covering the frequency range of interest. Bidimensional spatial Fourier transforms of the field maps, as well as spatial noise filtering, are carried out directly in MATLAB and allow us to extract IFCs and their corresponding loss distribution from the experimental data. The experimental hyperbolic band covers the frequencies between $f_1 \approx 8.8$ kHz and $f_2 \approx 11$ kHz. Albeit slightly higher in frequency than the pillar system simulations, due to sample fabrication inaccuracies, the results are in good agreement.

APPENDIX B: SIMULATION PROTOCOL

The simulation results of pillared metasurface presented in this paper are obtained with both the eigenfrequency module and the frequency response module of COMSOL Multiphysics Solid Mechanics for the band structure results [Figs. S3(a) and S3(b) in Supplemental Material [50] and point-source excitation of the finite-size sample [Figs. 2(d), 3(e), 4(c), 4(f), 5(b), and Supplemental Material Figs. S2(c) and S2(d) [50], respectively. The PLA material properties used are $E \approx 2.5$ GPa, $E \approx 2.5$ GPa, $\upsilon \approx 0.3$, and $\rho \approx 1300$ kg m^{-3}, and the material dissipation is modeled in COMSOL Multiphysics as a built-in isotropic loss factor $\eta_{\text{loss}} = 0.05$ such that the lossy elasticity tensor reads $C_{\text{loss}} = (1 + i\eta_{\text{loss}})C$. The simulated system consists of a single plate with a thickness 2.6 mm decorated with a square lattice of pillars on each side whose heights and global orientation depend on the side, with geometrical parameters similar to the ones of Appendix A. This design ensures the strong coupling between the two twisted lattices and the relevance of the homogenization procedure. In that regard, it differs from the experimental implementation where this strong coupling is practically obtained with double-sided tape which, albeit making the experiment straightforward and reconfigurable, induces additional dissipation in the system (see Supplemental Material Sec. III for more details [50]). For the finite-sample point-source simulations, perfectly matched layers are displayed around the metasurface that has a diameter of 51 unit cells. A point load with an out-of-plane total force is set at the center of the system, on the bottom side only, in order to excite efficiently the flexural waves in the plate. At a given operating frequency, the corresponding out-of-plane displacement 2D field maps on the bottom side of the plate is recorded, and using a 2D spatial Fourier transform in the MATLAB environment, we extract the corresponding IFC in reciprocal space. These results show good qualitative agreement with the experiments.

Simulations related to the homogenized metasurface [Figs. 1(d), 1(e), 1(g), 1(h), and 3(d)] are obtained by solving the corresponding partial differential equation problem at a given frequency using the Mathematics module of COMSOL for a 2D medium in the case of a point-source excitation. Similar to the pillar metasurface simulation described in the previous paragraph, a 2D spatial Fourier transform is applied using the MATLAB environment to the field map for contour extraction. Overall, a good qualitative agreement is reached between effective-medium theory, pillar metasurface simulations, and experiments.

APPENDIX C: THEORETICAL MODEL OF GENERAL HOMOGENIZED SHEAR-HYPERBOLIC METASURFACE

Here we provide a simple derivation of the model demonstrated in Fig. 1 for the case of magnetostatics. We start from Gauss's law for an isotropic medium:

$$\boldsymbol{\nabla} \cdot (\hat{\varepsilon}\mathbf{E}) = \boldsymbol{\nabla} \cdot \hat{\varepsilon}\left(-\boldsymbol{\nabla}\varphi - \frac{\partial \mathbf{A}}{\partial t}\right) = 0, \qquad \text{(C1)}$$

where we substitute the standard expression for the electric field in terms of the scalar and vector electromagnetic potentials φ and $\mathbf{A}$. We now apply the anisotropic form of the Lorenz gauge [59]

$$\nabla \cdot (\hat{\varepsilon}\mathbf{A}) = -\frac{\partial \phi}{\partial t} \tag{C2}$$

and substitute the left-hand side into Eq. (C1). Assuming, that $\hat{\varepsilon}$ is constant in time, it commutes with the time derivative, so that Eq. (C2) becomes

$$\nabla \cdot (\hat{\varepsilon}\nabla\varphi) - \frac{\partial^2 \varphi}{\partial t^2} = 0. \tag{C3}$$

Interestingly, this model coincides exactly with the Kirchoff-Love case if the nonlocal bi-Laplacian term is ignored. To evaluate loss, in our elasticity calculations we compute the scalar product $\nabla w^\dagger \mathfrak{I}[\hat{\tau}^\dagger]\nabla w$ (where w is the flexural displacement of the plate), which quantifies the effect of resonant loss within the medium, paralleling the standard expression $\mathbf{E}^\dagger \mathfrak{I}[\hat{\varepsilon}^\dagger]\mathbf{E}$ used for power loss rate in electrodynamics.

APPENDIX D: DERIVATION OF AXIAL DISPERSION AND SHEAR FACTOR

Diagonalization of $\mathfrak{R}[\hat{\tau}]$ gives the angle β that its two eigenvectors form with the x and y axes:

$$\beta = \frac{1}{2}\arctan\left(\frac{\Re[\tau_2]\sin(2\theta)}{\Re[\tau_1] + \Re[\tau_2]\cos(2\theta)}\right), \tag{D1}$$

Rotating the entire $\hat{\tau}$ tensor by β gives

$$\hat{\tau}' = \begin{pmatrix} \tau'_{xx} & \tau'_{xy} \\ \tau'_{yx} & \tau'_{yy} \end{pmatrix} = \begin{pmatrix} \Re[\tau'_{xx}] & 0 \\ 0 & \Re[\tau'_{yy}] \end{pmatrix} + i\begin{pmatrix} \Im[\tau'_{xx}] & \Im[\tau'_{xy}] \\ \Im[\tau'_{yx}] & \Im[\tau'_{yy}] \end{pmatrix}. \tag{D2}$$

With

$$\begin{aligned} \tau'_{xx} &= \tau_1 \cos^2(\beta) + \tau_2 \cos^2(\beta - \theta), \\ \tau'_{yy} &= \tau_1 \sin^2(\beta) + \tau_2 \sin^2(\beta - \theta), \\ \tau'_{xy} &= \{\sin(2\beta) I[\tau_1] + \sin[2(\beta - \theta)] I[\tau_2]\}/2. \end{aligned} \tag{D3}$$

τ'_{xy} can be normalized to 1 to obtain the shear coefficient

$$S(\omega, \theta) = \frac{\tau'_{xy}}{N^I} = \frac{\sin(2\beta)\mathfrak{I}[\tau_1] + \sin[2(\beta - \theta)]\mathfrak{I}[\tau_2]}{\mathfrak{I}[\tau_1] + \mathfrak{I}[\tau_2]} \tag{D4}$$

plotted in Fig. 3(b) of the main text, where we define the normalization factor $N^I = (\mathfrak{I}[\tau_1] + \mathfrak{I}[\tau_2])/2$. Note that the shear coefficient $S(\omega, \theta)$ is independent of the absolute losses in the system, as can be seen by multiplying $\mathfrak{I}[\tau_1]$ and $\mathfrak{I}[\tau_2]$ by a common factor, and it is therefore applicable to any wave phenomenon, frequency range, and loss level.

[1] A. Poddubny, I. Iorsh, P. Belov, and Y. Kivshar, *Hyperbolic metamaterials*, Nat. Photonics **7**, 948 (2013).

[2] Z. Liu, H. Lee, Y. Xiong, C. Sun, and X. Zhang, *Far-field optical hyperlens magnifying sub-diffraction-limited objects*, Science **315**, 1686 (2007).

[3] C. Shen, Y. Xie, N. Sui, W. Wang, S. A. Cummer, and Y. Jing, *Broadband acoustic hyperbolic metamaterial*, Phys. Rev. Lett. **115**, 254301 (2015).

[4] J. H. Oh, H. M. Seung, and Y. Y. Kim, *A truly hyperbolic elastic metamaterial lens*, Appl. Phys. Lett. **104**, 073503 (2014).

[5] Q. Zhang, G. Hu, W. Ma, P. Li, A. Krasnok, R. Hillenbrand, A. Alù, and C.-W. Qiu, *Interface nano-optics with van der Waals polaritons*, Nature (London) **597**, 187 (2021).

[6] Y. Wu, J. Duan, W. Ma, Q. Ou, P. Li, P. Alonso-González, J. D. Caldwell, and Q. Bao, *Manipulating polaritons at the extreme scale in van der Waals materials*, Nat. Rev. Phys. **4**, 578 (2022).

[7] W. Ma *et al.*, *Ghost hyperbolic surface polaritons in bulk anisotropic crystals*, Nature (London) **596**, 362 (2021).

[8] J. Taboada-Gutiérrez *et al.*, *Broad spectral tuning of ultra-low-loss polaritons in a van der Waals crystal by intercalation*, Nat. Mater. **19**, 964 (2020).

[9] A. J. Sternbach *et al.*, *Programmable hyperbolic polaritons in van der Waals semiconductors*, Science **371**, 617 (2021).

[10] Z. Zheng *et al.*, *A mid-infrared biaxial hyperbolic van der Waals crystal*, Sci. Adv. **5**, eaav8690 (2019).

[11] S. Dai *et al.*, *Tunable phonon polaritons in atomically thin van der Waals crystals of boron nitride*, Science **343**, 1125 (2014).

[12] N. C. Passler *et al.*, *Hyperbolic shear polaritons in low-symmetry crystals*, Nature (London) **602**, 595 (2022).

[13] G. Hu *et al.*, *Real-space nanoimaging of hyperbolic shear polaritons in a monoclinic crystal*, Nat. Nanotechnol. **18**, 64 (2023).

[14] J. Matson *et al.*, *Controlling the propagation asymmetry of hyperbolic shear polaritons in beta-gallium oxide*, Nat. Commun. **14**, 5240 (2023).

[15] A. A. High, R. C. Devlin, A. Dibos, M. Polking, D. S. Wild, J. Perczel, N. P. de Leon, M. D. Lukin, and H. Park, *Visible-frequency hyperbolic metasurface*, Nature (London) **522**, 192 (2015).

[16] P. Li, I. Dolado, F. J. Alfaro-Mozaz, F. Casanova, L. E. Hueso, S. Liu, J. H. Edgar, A. Y. Nikitin, S. Vélez, and R. Hillenbrand, *Infrared hyperbolic metasurface based on nanostructured van der Waals materials*, Science **359**, 892 (2018).

[17] J. S. Gomez-Diaz, M. Tymchenko, and A. Alù, *Hyperbolic plasmons and topological transitions over uniaxial metasurfaces*, Phys. Rev. Lett. **114**, 233901 (2015).

[18] L. Quan and A. Alù, *Hyperbolic sound propagation over nonlocal acoustic metasurfaces*, Phys. Rev. Lett. **123**, 244303 (2019).

[19] E. Martini, F. Giusti, A. Benini, and S. Maci, *Dual-mode hyperbolicity, supercanalization, and leakage in self-complementary metasurfaces*, Nanophotonics **12**, 2973 (2023).

[20] S. Carr, D. Massatt, S. Fang, P. Cazeaux, M. Luskin, and E. Kaxiras, *Twistronics: Manipulating the electronic properties of two-dimensional layered structures through their twist angle*, Phys. Rev. B **95**, 075420 (2017).

[21] Y. Cao, V. Fatemi, S. Fang, K. Watanabe, T. Taniguchi, E. Kaxiras, and P. Jarillo-Herrero, *Unconventional superconductivity in magic-angle graphene superlattices*, Nature (London) **556**, 43 (2018).

[22] P. Rickhaus *et al.*, *Correlated electron-hole state in twisted double-bilayer graphene*, Science **373**, 1257 (2021).

[23] Q. Tong, H. Yu, Q. Zhu, Y. Wang, X. Xu, and W. Yao, *Topological mosaics in moiré superlattices of van der Waals heterobilayers*, Nat. Phys. **13**, 356 (2017).

[24] F. Wu, T. Lovorn, and A. H. MacDonald, *Topological exciton bands in moiré heterojunctions*, Phys. Rev. Lett. **118**, 147401 (2017).

[25] A. Ciarrocchi, F. Tagarelli, A. Avsar, and A. Kis, *Excitonic devices with van der Waals heterostructures: Valleytronics meets twistronics*, Nat. Rev. Mater. **7**, 449 (2022).

[26] W. Chen, Z. Sun, Z. Wang, L. Gu, X. Xu, S. Wu, and C. Gao, *Direct observation of van der Waals stacking-dependent interlayer magnetism*, Science **366**, 983 (2019).

[27] B. Lou, N. Zhao, M. Minkov, C. Guo, M. Orenstein, and S. Fan, *Theory for twisted bilayer photonic crystal slabs*, Phys. Rev. Lett. **126**, 136101 (2021).

[28] K. Dong, T. Zhang, J. Li, Q. Wang, F. Yang, Y. Rho, D. Wang, C. P. Grigoropoulos, J. Wu, and J. Yao, *Flat bands in magic-angle bilayer photonic crystals at small twists*, Phys. Rev. Lett. **126**, 223601 (2021).

[29] M. Oudich, G. Su, Y. Deng, W. Benalcazar, R. Huang, N. J. R. K. Gerard, M. Lu, P. Zhan, and Y. Jing, *Photonic analog of bilayer graphene*, Phys. Rev. B **103**, 214311 (2021).

[30] P. Wang, Y. Zheng, X. Chen, C. Huang, Y. V. Kartashov, L. Torner, V. V. Konotop, and F. Ye, *Localization and delocalization of light in photonic moiré lattices*, Nature (London) **577**, 42 (2020).

[31] G. Hu, A. Krasnok, Y. Mazor, C.-W. Qiu, and A. Alù, *Moiré hyperbolic metasurfaces*, Nano Lett. **20**, 3217 (2020).

[32] G. Hu *et al.*, *Topological polaritons and photonic magic angles in twisted α-*MoO_3 *bilayers*, Nature (London) **582**, 209 (2020).

[33] M.-I. Cohen, C. Jörg, Y. Lumer, Y. Plotnik, E. H. Waller, J. Schulz, G. von Freymann, and M. Segev, *Generalized laws of refraction and reflection at interfaces between different photonic artificial gauge fields*, Light **9**, 200 (2020).

[34] M. Chen, X. Lin, T. H. Dinh, Z. Zheng, J. Shen, Q. Ma, H. Chen, P. Jarillo-Herrero, and S. Dai, *Configurable phonon polaritons in twisted α-*MoO_3, Nat. Mater. **19**, 1307 (2020).

[35] J. Duan, N. Capote-Robayna, J. Taboada-Gutiérrez, G. Álvarez-Pérez, I. Prieto, J. Martín-Sánchez, A. Y. Nikitin, and P. Alonso-González, *Twisted nano-optics: Manipulating light at the nanoscale with twisted phonon polaritonic slabs*, Nano Lett. **20**, 5323 (2020).

[36] Q. Fu, P. Wang, C. Huang, Y. V. Kartashov, L. Torner, V. V. Konotop, and F. Ye, *Optical soliton formation controlled by angle twisting in photonic moiré lattices*, Nat. Photonics **14**, 663 (2020).

[37] Y. Deng, M. Oudich, N. J. R. K. Gerard, J. Ji, M. Lu, and Y. Jing, *Magic-angle bilayer phononic graphene*, Phys. Rev. B **102**, 180304 (2020).

[38] M. Oudich, Y. Deng, and Y. Jing, *Twisted pillared phononic crystal plates*, Appl. Phys. Lett. **120**, 232202 (2022).

[39] S. M. Gardezi, H. Pirie, S. Carr, W. Dorrell, and J. E. Hoffman, *Simulating twistronics in acoustic metamaterials*, 2D Mater. **8**, 031002 (2021).

[40] M. Martí-Sabaté and D. Torrent, *Dipolar localization of waves in twisted phononic crystal plates*, Phys. Rev. Appl. **15**, L011001 (2021).

[41] S. Yves, M. I. N. Rosa, Y. Guo, M. Gupta, M. Ruzzene, and A. Alù, *Moiré-driven topological transitions and extreme anisotropy in elastic metasurfaces*, Adv. Sci. **9**, 2200181 (2022).

[42] Y. Yang, Y. Ge, R. Li, X. Lin, D. Jia, Y.-j. Guan, S.-q. Yuan, H.-x. Sun, Y. Chong, and B. Zhang, *Demonstration of negative refraction induced by synthetic gauge fields*, Sci. Adv. **7**, eabj2062 (2021).

[43] M. I. N. Rosa, M. Ruzzene, and E. Prodan, *Topological gaps by twisting*, Commun. Phys. **4**, 130 (2021).

[44] S. Yves, Y.-G. Peng, and A. Alù, *Topological Lifshitz transition in twisted hyperbolic acoustic metasurfaces*, Appl. Phys. Lett. **121**, 122201 (2022).

[45] M. Rosendo López, F. Peñaranda, J. Christensen, and P. San-Jose, *Flat bands in magic-angle vibrating plates*, Phys. Rev. Lett. **125**, 214301 (2020).

[46] Y. Jin, Y. Pennec, B. Bonello, H. Honarvar, L. Dobrzynski, B. Djafari-Rouhani, and M. I. Hussein, *Physics of surface vibrational resonances: Pillared phononic crystals, metamaterials, and metasurfaces*, Rep. Prog. Phys. **84**, 086502 (2021).

[47] P. Roux *et al.*, *Toward seismic metamaterials: The META-FORET project*, Seismol. Res. Lett. **89**, 582 (2018).

[48] S. Brûlé, S. Enoch, and S. Guenneau, *Emergence of seismic metamaterials: Current state and future perspectives*, Phys. Lett. A **384**, 126034 (2020).

[49] S. H. Sedighy, C. Guclu, S. Campione, M. K. Amirhosseini, and F. Capolino, *Wideband planar transmission line hyperbolic metamaterial for subwavelength focusing and resolution*, IEEE Trans. Microwave Theory Tech. **61**, 4110 (2013).

[50] See Supplemental Material at http://link.aps.org/supplemental/10.1103/PhysRevX.14.021031, which includes Refs. [51–53] for (i) the theoretical model of the homogenized elastic metasurface, (ii) an analytical solution of the Kirchoff-Love equation, (iii) a validation of the shear factor S against momentum-dependent measurements, and (iv) the behavior in the small-angle limit. Additional figures on the experimental setup, numerical simulations, and defect detection protocol are referenced in the main text.

[51] K. F. Graff, *Wave Motion in Elastic Solids* (Dover Publications, Inc., New York, 1991).

[52] W. Wang, B. Bonello, B. Djafari-Rouhani, Y. Pennec, and J. Zhao, *Double-negative pillared elastic metamaterial*, Phys. Rev. Appl. **10**, 064011 (2018).

[53] D. Qian and Z. Shi, *Bandgap properties in simplified model of composite locally resonant phononic crystal plate*, Phys. Lett. A **381**, 3505 (2017).

[54] H. Hu *et al.*, *Gate-tunable negative refraction of mid-infrared polaritons*, Science **379**, 558 (2023).

[55] A. J. Sternbach *et al.*, *Negative refraction in hyperbolic hetero-bicrystals*, Science **379**, 555 (2023).

[56] H. He, C. Qiu, L. Ye, X. Cai, X. Fan, M. Ke, F. Zhang, and Z. Liu, *Topological negative refraction of surface acoustic waves in a Weyl phononic crystal*, Nature (London) **560**, 61 (2018).

[57] M. Lott, P. Roux, L. Seydoux, B. Tallon, A. Pelat, S. Skipetrov, and A. Colombi, *Localized modes on a metasurface through multiwave interactions*, Phys. Rev. Mater. **4**, 065203 (2020).

[58] H. Tang, B. Lou, F. Du, G. Gao, M. Zhang, and X. Ni, and E. Mazur, *On-chip multidimensional dynamic control of twisted moiré photonic crystal for smart sensing and imaging*, arXiv:2312.09089.

[59] B. R. Chawla, S. S. Rao, and H. Unz, *Potential equations for anisotropic inhomogeneous media*, Proc. IEEE **55**, 421 (1967).